



# Production of Nickel by Cold Hydrogen Plasma

Kali Charan Sabat<sup>1</sup>

Received: 6 May 2021 / Accepted: 17 June 2021 / Published online: 28 June 2021

© The Author(s), under exclusive licence to Springer Science+Business Media, LLC, part of Springer Nature 2021

## Abstract

Recently, a new production process of various metals and alloys from their oxides and ores by Cold Hydrogen Plasma (CHP) has been introduced. CHP is produced by using a microwave oven, using less power than the microwave ovens used domestically for cooking food. CHP is very efficient in producing metals and alloys from their oxides because of excited species. These excited species decrease the thermodynamic and kinetic barriers of reduction, making the reduction easier and faster. In the current investigation, nickel has been produced from nickel oxide (NiO) pellets of ~2.5 gm to ~7.5 gm. The hydrogen flow rate ranges from 70 ml/s to 150 ml/s, and power varies from 600 to 750 W. The time taken for reduction changed between 300 to 1200 s. CHP reduces very fast due to the active oxygen present in it. This faster production of nickel from pellets upto ~7.5 gm at such low power opens up the possibilities of upscaling the reduction of NiO by CHP.

**Keywords** Production of nickel · Thermodynamics · Kinetics · Cold hydrogen plasma · Excess oxygen

## Introduction

Due to the essential properties such as high melting point, a right combination of strength and ductility, good resistance to high-temperature oxidation and general corrosion, nickel stands as a strategically crucial alloying element for chemical processing industries, space research, and nuclear reactor engineering. Apart from all these applications, it is also used as a catalyst. Nickel consumption worldwide has reached 2.7 million tonnes/year [1]. It comes from 2 types of ores: (a) Oxide ores, and (b) Sulphide ores [1]. Nickel is mainly extracted from the oxide ores (referred to as nickeliferous laterites) [2–5]. The oxide ores generally consist of 2 layers, namely, Limonite (0.8–1.5% Ni, 40–50% Fe, 0.5–5% MgO) and Saprolite (1.8–5% Ni, 10–25% Fe, 15–35% MgO) [1, 6]. These two layers vary in chemical composition and mineralogy. Due to these variations, a standard extraction flow sheet cannot be applied to both, and hence, nickel is extracted from these ores by different process routes. The process route of nickel production involves pyrometallurgical, hydrometallurgical, or a mixture of both [7].

✉ Kali Charan Sabat  
kcsabat@gmail.com; drkcsabat@manit.ac.in

<sup>1</sup> Department of Materials and Metallurgical Engineering, Maulana Azad National Institute of Technology, Bhopal 462003, Madhya Pradesh, India

Whatever the process route may be, intermediate products are produced. The intermediate products are generally nickel carbonates, nickel hydroxides, nickel oxides, etc. These intermediate products are reduced to crude nickel by reducing agents such as carbon monoxide, hydrogen, etc. [1, 5, 8–15].

Hydrogen ( $H_2$ ) is preferred as a reducing agent for the reduction of the intermediate products due to the following reasons: (a) it is environmental friendly, (b) provides faster kinetics, (c) gives rise to a final product with high purity [16]. For example, in the conventional well known Caron's process, Basic Nickel Carbonate (BNC) is decomposed to NiO, which is subsequently reduced to high-grade nickel by  $H_2$ , in the nickel refinery at BHP Billiton, Yabulu refinery, Australia [17]. Reduction of NiO produced from pyrohydrolysis of chloride solutions [18] is carried out at the Goro-Nickel plant at Noumea. Another example is the roasting of the pelletized sulfide concentrate to produce NiO, followed by reduction with  $H_2$  [19]. Although  $H_2$  has several advantages, it is associated with a little bit of thermodynamics and kinetic limitations, as well as some safety aspects like risk of explosion in contact with air/oxygen, etc. The thermodynamic restriction comes from the less negative value of  $\Delta G$  of reduction of NiO by  $H_2$ . The kinetic limitations are: (a) persistence of the incubation period since the pioneering work by Benton et al. [20], (b) extensive variation of activation energy (more than one order), reviewed by L'Vov et al. [21], and reported by other researchers [11, 22–25], (c) applications of different kinetic models to describe this reaction [23, 26]. However, recently, cold hydrogen plasma (CHP) could overcome the thermodynamic and kinetic (e.g., diffusion) limitations for the production of metals and alloys from their oxides [27–33] or mixture of oxides [32, 34, 35], due to the presence of excited species. The following facts are well established from these investigations: (a) the excited plasma species decrease the  $\Delta G^\circ$ , (b) successful reduction occurred with a decrease in activation energy due to CHP's activated plasma species, (c) further, it is argued based on the thermodynamic data that the equilibrium partial pressure of atomic hydrogen (H) needed to reduce these metal oxides decreases with decrease in temperature. This decrease of the equilibrium partial pressure with decrease in temperature is sharper for H in comparison to  $H_2$ . This sharp decrease indicates that the reduction reactions are favorable at low temperature by CHP, due to the presence of H. The underlying question is whether the CHP having H and other excited plasma species can reduce the non-stoichiometric oxide  $Ni_{1-x}O$ .

The motivation for the current investigation of the reduction of NiO by CHP is based on the following reasons: (a) plasma uses are becoming more prevalent in metallurgical processes, including metal extraction [10, 27, 36–54]. (b) the extraction flow sheet of nickel production includes a unit process of reduction of an intermediate product, e.g., NiO, (c)  $NiO \rightarrow Ni$  is a single-step process whereas other metal oxides show multi-step reduction, (d)  $NiO \rightarrow Ni$  reduction process is only slightly exothermic, therefore, can be considered as isothermal, whereas, other metal oxides had contributions to reaction enthalpy, (e)  $NiO \rightarrow Ni$  reduction is irreversible and first order with respect to  $H_2$ . (f) associated with only minor structural changes (g) to check whether there is any effect of stoichiometry on the plasma-metal oxide reaction, (h) to check whether CHP can remove the persistent incubation period.

## Experimental Details

The experimental details pertinent to the CHP, the procedure of preparation of compacted pellets from metal oxide powders, the experimental set-up, and the experimental approach have been already discussed in the earlier publications [27, 28, 36]. However, for readers'

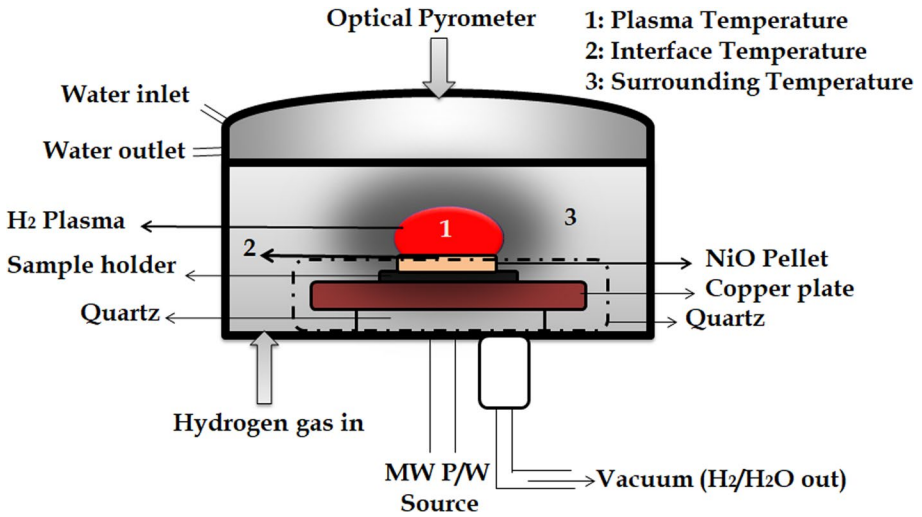


Fig. 1 The schematic of the microwave plasma reactor

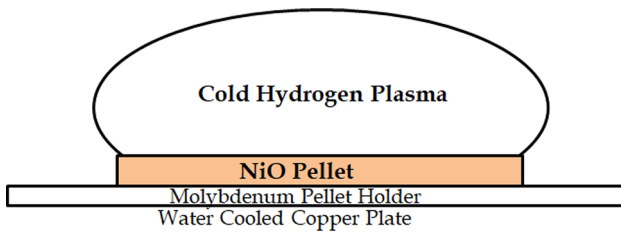


Fig. 2 Magnified view of the sample with the plasma region of Fig. 1

understanding, the schematic of the CHP reactor used in the current investigation has been reproduced in Fig. 1. It consists of two parts. The top part is the reduction chamber, where CHP is created, and reduction occurs at the CHP-pellet interface. The bottom part is the operation rack, which controls the operating parameters of the experiment. The reduction chamber is made of aluminium alloy and cylindrical (~0.4 m diameter and ~0.1 m height). It is double-walled, in which the chilled water flows to keep the surface temperature at room temperature.

However, there is no external heating of the reactor chamber. Therefore, no volumetric heating of H<sub>2</sub> inside the reduction chamber. The heating takes place due to local heating by CHP at the CHP-pellet reduction interface, whose magnified view as shown in Fig. 2, whose discussion follows.

The pellet is cylindrical, with a diameter of  $20 \times 10^{-3}$  m and heights ranging from  $2 \times 10^{-3}$  m to  $6 \times 10^{-3}$  m. The pellet is placed on the pellet holder made of molybdenum. The pellet holder is put at the center of the reduction chamber. To avoid the heating of the pellet holder during the experiment, it is placed above a water-cooled copper plate. Surrounding the copper plate, a quartz ring is provided to help the CHP focusing on the pellet. After placing the pellet inside the reduction chamber, the chamber is closed. Then the chamber is evacuated by the rotary pump till the chamber pressure

reaches 0.1 Pa. After removal of the unwanted gaseous species,  $H_2$  is injected through an inlet located at the chamber wall, into the reduction chamber, at the desired flow rate required for the experiment. After a particular gas pressure is reached inside the chamber, the microwave is switched on. The microwave generator generates microwaves at a frequency of  $2.45 \times 10^9 \text{ s}^{-1}$ . The  $H_2$ , having little polarity, interacts with the high-frequency electromagnetic field of the microwave. Due to this interaction,  $H_2$  gets excited to produce excited species that constitute the CHP. The CHP is controlled by microwave power and chamber pressure. It is primarily spherical. But when CHP interacts with the pellet, it becomes elliptical and covers the pellet's upper flat surface, as shown in Fig. 2. The reduction starts from the pellet's top flat surface, where CHP comes in contact with the pellet. As mentioned earlier, whatever the heating takes place inside the reactor, it is only due to the heat produced by CHP at the CHP-pellet interface [29, 32, 34, 35, 55].

The NiO powder used for making the pellets in the present study was sourced from J. T. Baker Ltd. The powder was subjected to phase analysis using X'Pert PRO-PANalytical (Model No—3,040,160). The XRD is shown in Fig. 3.

The XRD analysis of nickel oxide showed that NiO used is pure, as per JCPDS file no JCPDS-00-047-1049. It doesn't contain Ni or any other nickel oxide phases like  $Ni_2O_3$ . The temperature, pressure,  $H_2$  flow rate, microwave power, etc., were adequately monitored throughout the experiments. After each experiment, the weight loss during reduction was measured with a digital weighing balance with an accuracy of  $0.1 \times 10^{-6} \text{ kg}$ . The quantitative estimation of the phases was carried out by Rietveld analysis and wet chemical analysis (iodometry). The details of Rietveld analysis and wet chemical analysis (iodometry) have been discussed later.

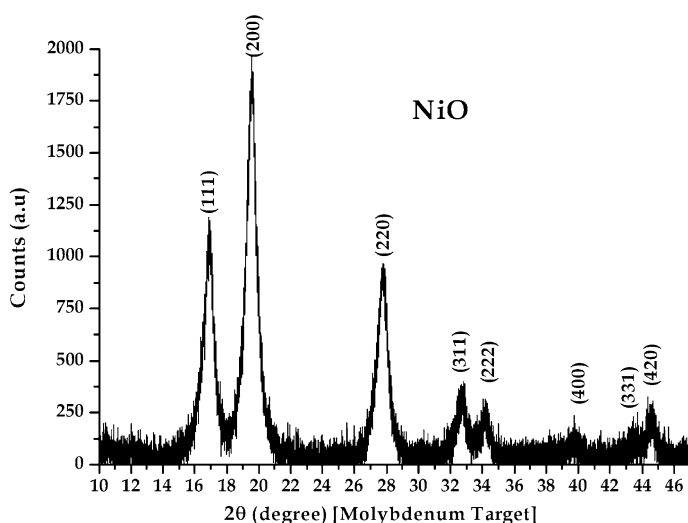
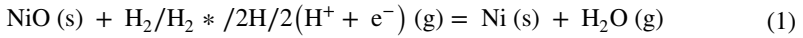


Fig. 3 XRD of the raw material of nickel oxide

## Results and discussion

### Thermodynamic feasibility

The CHP used for reduction consists of H<sub>2</sub> and various excited species such as H, ionic hydrogen (H<sup>+</sup>), and ro-vibrationally excited hydrogen molecules (H<sub>2</sub>\*). Accordingly, the reduction reaction can be written as:



Thermodynamics and kinetics are the potential pathways for the above reduction reaction. The thermodynamic feasibility is depicted by the Ellingham diagram (Fig. 4).

The figure is drawn using the following reactions of interest:

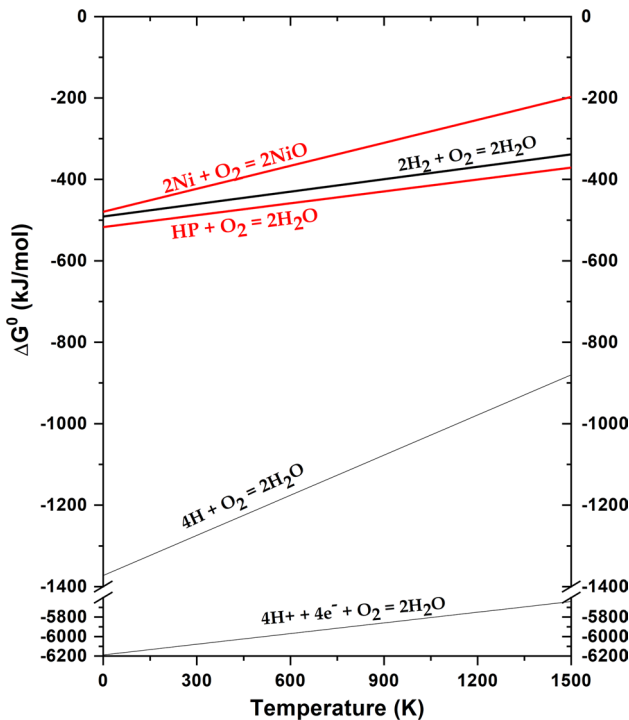
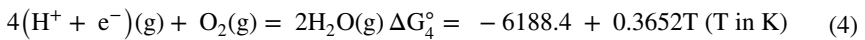
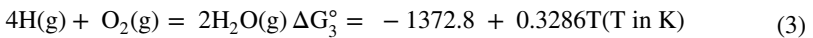
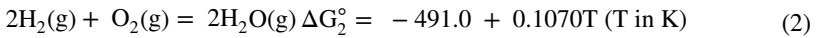


Fig. 4 Ellingham diagram for nickel—nickel oxide, H<sub>2</sub> – H<sub>2</sub>O and Hydrogen Plasma (HP)—H<sub>2</sub>O [36, 56, 61–63]

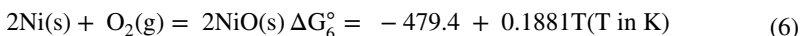
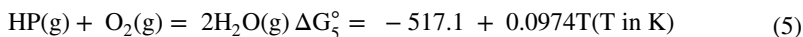
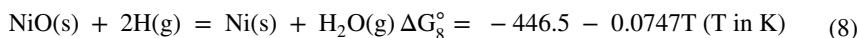


Figure 4 gives the relationship between the  $\Delta G^\circ$  and temperature (T), for the above reactions of Eqs. (2)–(6). The thermodynamic data for Eqs. (2)–(4) have been taken from NIST-JANAF database [56], which is a major compilation of thermodynamic experimental data obtained from various sources, e.g., [57–60]. Thermodynamic data for Eq. (5) has been estimated from the quantities of various species present in CHP. As reported earlier [36], Hydrogen plasma (HP) reduce the upper oxides. The more is in the current investigation consists of 2% H, 7.86%  $\text{H}_2^*$  ( $\nu=1$  level), 0.35%  $\text{H}_2^*$  ( $\nu=2$  level), with the remaining 89.79% being ground-state  $\text{H}_2$ . The estimated  $\Delta G^\circ$  for HP, is shown in Fig. 4. As evident from Fig. 4, the  $\Delta G^\circ$  decreases around 26 kJ/mol due to the presence of HP.

However, thermodynamic data for Eq. (6) was not available in NIST-JANAF database, therefore, Ni  $\rightarrow$  NiO data has been taken from another reference [61]. In this reference, authors have developed the equation for  $\Delta G^\circ$  of Ni  $\rightarrow$  NiO, after extensive comparison of  $\Delta G^\circ$  data of Ni  $\rightarrow$  NiO obtained from various electrochemical cells and chemical reduction/oxidation equilibrium measurements.

The Ellingham diagram principle is that the elements lying below in the diagram can reduce the upper oxides. The more is the  $\Delta G^\circ$  difference, the more is the feasibility of reduction. As shown in Fig. 4, the  $\text{H}_2 \rightarrow \text{H}_2\text{O}$  line lies just slightly below the Ni  $\rightarrow$  NiO line. However, the difference of  $\Delta G^\circ$  is only marginal ( $\Delta G^\circ$  difference varies from 5.82 kJ/mol at 0 K to 66.57 kJ/mol at 1500 K). This small difference of  $\Delta G^\circ$  at low temperature does not make  $\text{H}_2$  a better reductant at low temperature. However, the remarkable fact is that the H and  $\text{H}^+$  lines lay 650 kJ and 5700 kJ below the NiO line at all temperatures, indicating that H and  $\text{H}^+$  are more powerful reductants than  $\text{H}_2$ . Apart from these species and  $\text{H}_2$ , CHP also contains  $\text{H}_2^*$ , which also lowers the  $\Delta G^\circ$  value. These species present in HP lower the  $\Delta G^\circ$  value, confirming that  $\text{H}_2$  in the plasma state is more potent reductant than  $\text{H}_2$ . As estimated earlier, the lowering of  $\Delta G^\circ$  for the present plasma composition is 26 kJ/mol. The lowering of  $\Delta G^\circ$  due to HP has also been reported in earlier reports [32, 35, 36]. With CHP, the difference of  $\Delta G^\circ$  increases with increased temperature. The increased  $\Delta G^\circ$  ranges from 18.80 kJ/mol (at 0 K) to 86.70 kJ/mol (at 1500 K). Due to the presence of the excited species, the following reduction reactions occur in CHP:



The overall reaction is



The  $\Delta G^\circ$  versus T of these reduction reactions are shown in Fig. 5.

As evident from Fig. 5,  $\Delta G^\circ$  for the reduction by  $\text{H}_2$  (Eq. 7) is slightly negative, thus not supporting  $\text{H}_2$  as a potent reductant at low temperature. However,  $\Delta G^\circ$  for the reduction by HP (Eq. 9) is more negative, making HP a potent reductant even at low temperatures.

It is worth mentioning that the  $\Delta G^\circ$  values of these reduction reactions (Eqs. 7–9), as shown in Fig. 5, are functions of T and the associated equilibrium constant (K) of the reduction reaction. It is mathematically written as  $\Delta G^\circ = -RT \ln K$ . Considering  $K = p\text{H}_2\text{O}/$

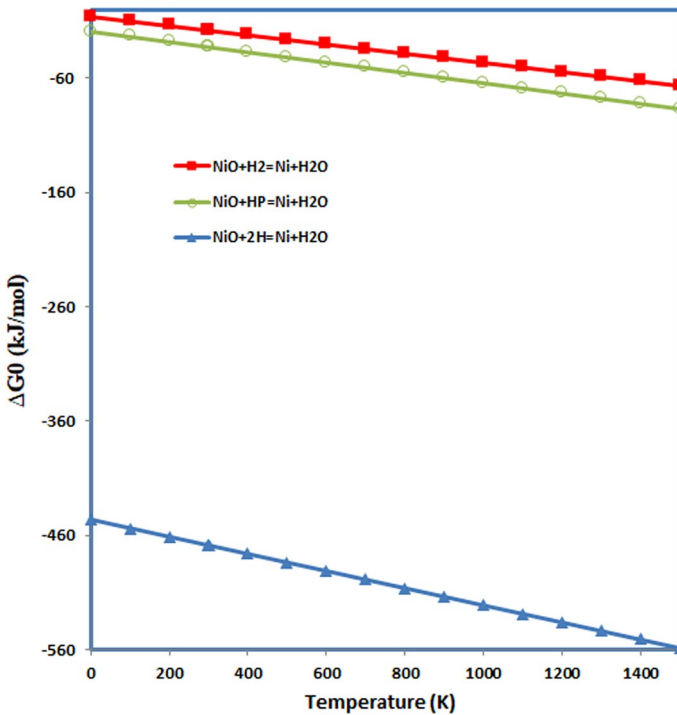


**Fig. 5** The  $\Delta G^\circ$  versus T plot for the reduction of NiO by  $H_2$  and HP estimated from references [36, 56, 61–63]

$pH_2$  in the case of  $H_2$  reduction and putting this value in the  $\Delta G^\circ$  expression and after simplifying, the B-G equilibrium diagram can be worked out [27, 29, 55]. Figure 6 shows the B-G diagram, which shows the equilibrium partial pressure of  $H_2$  or H, required at various NiO  $\rightarrow$  Ni reduction temperatures. The CHP temperature lies within the temperature range shown in Fig. 6.

The B-G diagram gives the necessary inferences. Firstly, the equilibrium partial pressure of  $H_2$ /H required for NiO  $\rightarrow$  Ni reduction decreases with a decrease in temperature, indicating favorable conditions at lower temperatures. Second, the decline is much sharper for H than the  $H_2$ , making H more potent than  $H_2$ . The excited molecular hydrogen ( $H_2^*$ ) is expected to come between  $H_2$  and H (Fig. 6). It is because  $H_2$  absorbs energy from the plasma electrons and stores the energy in the form of rotation and vibration, to form  $H_2^*$ , followed by dissociation to H. The  $\Delta G^\circ$  of  $H_2^*$  lies between  $\Delta G^\circ$  of  $H_2$  and H. Therefore,  $H_2^*$  line is expected to come between  $H_2$  and H, indicating that presence of  $H_2^*$  makes the reduction more feasible at low temperatures.

## Reduction Studies

After verifying the thermodynamic feasibility, the experiments were started with a  $\sim 2.5 \times 10^{-3}$  kg pellet with a diameter of  $2 \times 10^{-2}$  m. This size has already been used in earlier investigations [29, 32, 34, 35, 55]. The experimental results of the reduction are shown in Table 1. For the same pellet size ( $\sim 2.5 \times 10^{-3}$  kg, diameter  $2 \times 10^{-2}$  m), in the earlier

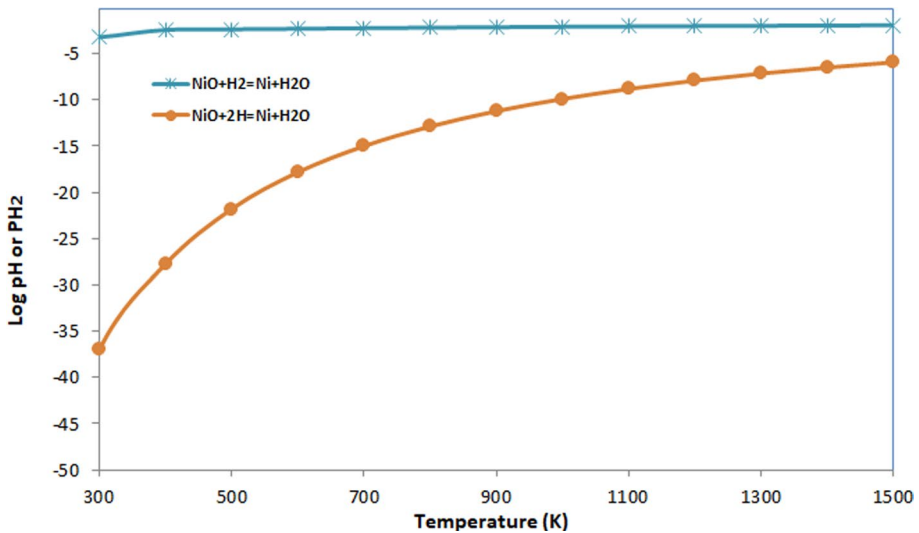


**Fig. 6** Bauer – Glaessner diagram of variation in hydrogen partial pressure with temperature [36, 56, 61–63]

**Table 1** Weight loss and percentage reduction from weight loss and Rietveld analysis

Samples	Power/W	Flow rate/sccm	Time/s	Initial weight/ 10 <sup>-3</sup> kg	Final weight/ 10 <sup>-3</sup> kg	Percentage reduction/ weight loss	Percentage reduction/ Rietveld
CuO[55]	750	150	1200	2.490	1.978	102	—
Fe <sub>2</sub> O <sub>3</sub> [32]	750	150	3600	2.461	2.075	52.1	—
NiO	750	150	3600	2.503	1.911	110	100
NiO	750	150	1200	2.576	1.941	115	100
NiO	750	150	300	2.512	1.904	113	100
NiO	750	70	300	2.492	1.931	105	91
NiO	600	70	1200	7.642	6.086	95	80

investigations, the time taken for reduction varied between 1200 to 3600 s [29, 32, 34, 35, 55]. The two extreme cases of time taken [32, 55] are given in Table 1, for comparison.

As shown in Table 1, under similar plasma operating parameters for  $\sim 2.5 \times 10^{-3}$  kg pellet, CuO reduces completely to copper at 1200 s, whereas Fe<sub>2</sub>O<sub>3</sub> could reduce only 52.1% at 3600 s. These were stoichiometric oxides. Therefore, the percentage reductions for these experiments were calculated from the ratio of weight loss to the initial stoichiometric amount of oxygen present in the sample. Due to the difficulty faced during the reduction of Fe<sub>2</sub>O<sub>3</sub> (i.e., Fe<sub>2</sub>O<sub>3</sub> could reduce only 52.1% at 3600 s, under the same operating conditions) and the  $\Delta G^\circ$  of reduction of NiO  $\rightarrow$  Ni by H<sub>2</sub> being very high in comparison to  $\Delta G^\circ$  of Fe<sub>2</sub>O<sub>3</sub>  $\rightarrow$  Fe by H<sub>2</sub>, the initial experiment was performed for 3600 s. The investigation was carried out for  $\sim 2.5 \times 10^{-3}$  kg pellet at a microwave power of 750 W and a flow rate of  $2.5 \times 10^{-6}$  m<sup>3</sup> s<sup>-1</sup>. After the experiment, the CHP was extinguished by switching off the microwave power. The reduced sample was allowed to cool in the reduction chamber. The



cooling of the reduced pellet is faster because the reduction chamber always remains at nearly room temperature. After cooling, the reduced pellet was taken out of the reduction chamber. The final weight was taken with  $0.1 \times 10^{-6}$  kg accuracy, and the pellet was kept in a desiccator with desiccant silica gel. As done earlier [27–29, 34, 35, 55], the percentage reduction was estimated from the ratio of weight loss to the theoretical amount of oxygen present in NiO.

Interestingly, the percentage reduction of the 3600 s sample estimated from weight loss was found to be 110%. Unexpectedly, this value is greater than 100%. Initially, it was thought that there might be some experimental errors or calculation mistakes. The error might be due to the absorption of moisture by the pellet. To avoid moisture absorption, the compacted NiO pellets were kept in a drying oven at 423 K for a day. This care was taken to remove the residual moisture and avoid moisture absorption. Also, there was no formation of other nickel oxides during drying. With this care, the experiment was performed for  $\sim 2.5 \times 10^{-3}$  kg for the 1200 s. Again, the estimated percentage reduction exceeded 100% (i.e., 115%). The XRD pattern is shown in Fig. 7(a). After that, the experiments were performed with a gradual decrease in the time for reduction from 1200 s to achieve the minimum time required for complete reduction.

Nevertheless, even after decreasing the reduction time, the percentage reduction estimated from weight loss was found to be more than 100% every time. Finally, for a reduction time of 300 s, more than 100% reduction by weight loss (i.e., 113%) was achieved. The XRD pattern is shown in Fig. 7(b). After that, no more experiments were carried out by reducing the time further. However, several experiments were done (e.g., Fig. 7(c) and 7(d)) to verify the techno-economic feasibility and application of rate equations as reported for other metal oxides [28, 29, 32, 34, 35, 55]. For example, Johnson and Mehl, Avrami, and Erofeev equation [34, 35, 55], moving-interface [29], Arrhenius equation [28], and other rate equations. None of the rate equations fitted into the experimental data.

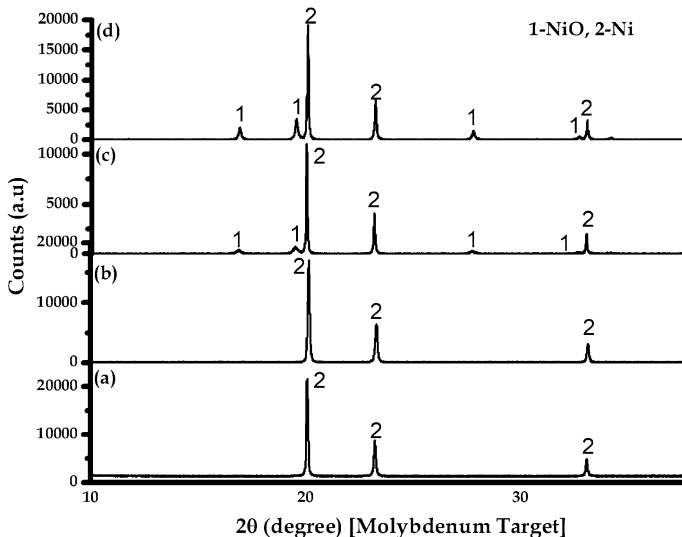


**Fig. 7** XRD patterns of the reduction product (Nickel) at various pellet size, flow rates of hydrogen, microwave power, and time, **a**  $2.576 \times 10^{-3}$  kg,  $150 \times 10^{-6} \text{ m}^3 \text{ s}^{-1}$ , 750 W, and 1200 s, **b**  $2.512 \times 10^{-3}$  kg,  $150 \times 10^{-6} \text{ m}^3 \text{ s}^{-1}$ , 750 W, and 300 s, **c**  $2.492 \times 10^{-3}$  kg,  $70 \times 10^{-6} \text{ m}^3 \text{ s}^{-1}$ , 750 W, and 300 s, **d**  $7.642 \times 10^{-3}$  kg,  $70 \times 10^{-6} \text{ m}^3 \text{ s}^{-1}$ , 600 W, and 1200 s

Also, the results of more than 100% reduction (Table. 1) seems quite confusing, although the total oxygen concentration in NiO was precisely evaluated. This is because the oxygen content of the surface and bulk of the pellet is not the same. Lattice excess oxygen contributes more at the bulk, whereas the surface gets contribution both from surface excess oxygen and lattice excess oxygen. So the excess oxygen at the surface and bulk are not the same. Therefore, even after precisely evaluating the oxygen concentration in NiO, the weight loss exceeds 100%. Thus, instead of calculating the percentage reduction from weight loss, the percentages reduction was estimated using Rietveld analysis.

Due to the repeated results of more than 100% reduction obtained from the weight loss calculation, the percentage reduction was also estimated by quantitative XRD by Rietveld analysis using (space group Fm-3 m (225)) X'Pert HighScore Plus. The Rietveld analysis is a powerful quantitative technique in XRD, which estimates several parameters from XRD data, *e.g.*, phase quantities (Ni and NiO in the present study), the crystallite sizes, micro strain in crystal lattices, bond lengths, texture, vacancies, etc. [64]. The Rietveld analysis develops a structural model from the atomic structure data (*e.g.*, unit cell dimensions, etc.) and instrumental parameters, which fits a calculated experimental data profile by employing the non-linear least-squares method. The quantitative phase analysis result showed complete Ni, implying a 100% reduction at 300 s. However, the repeated results of more than 100% reduction gave rise to the possibility of extra oxygen in NiO. Also, rate equations derived in the previous publications on various metal oxides and their mixtures [29, 32, 34, 35, 55] were tried to fit the experimental data of NiO, but these rate equations didn't fit with the experimental data. As a result, non-stoichiometric and thus excess oxygen became an issue.

To investigate the presence of excess oxygen and its source, a literature search was done. It was found that Deren and Stoch [65] have analyzed the presence of extra oxygen in the experimental results of 18 researchers. They examined the effect of oxygen on the stoichiometric composition of nickel oxide. Also, they examined the effect of oxygen on the chemisorption properties of the surface and the bulk of NiO. They concluded that NiO is always associated with excess oxygen. The extra oxygen content depends on the processing route. This extra oxygen comes from two sources: (a) the chemisorbed oxygen from the surface, (b) the excess oxygen present in lattice. To avoid the confusion between the two, they [65] proposed a new term, 'active oxygen,' which is written as:

Active oxygen = lattice excess oxygen + surface excess oxygen.

Out of these two components of active oxygen, most oxygen comes from the surface excess oxygen, which is removed easily compared to the lattice excess oxygen [60]. The present study is mainly concerned with the removal of oxygen from the crystal lattice of NiO. Therefore, in order to examine the presence of lattice excess oxygen and its effect on reduction, XRD analysis was carried out.

## XRD Analysis

The XRD analysis of the raw NiO sample was done with a molybdenum target [27, 29, 32, 34, 55] over a  $2\theta$  range of 10–47 (Fig. 3). Figure 3 shows a huge fluorescence in the background and peak broadening. Initially, it was thought that it might be due to the molybdenum target for the NiO sample. Therefore, the target material was changed to copper. Surprisingly, the same phenomenon was observed, *i.e.*, fluorescence and peak broadening. The huge fluorescence from both the targets ruled out the possibility of fluorescence from the target material. Therefore, subsequent XRDs were carried out with the molybdenum

target, as used in earlier investigations [29, 32, 34, 35, 55]. However, to avoid noise, a long scan time (80 s) and a small step size (0.0170°) was taken. Despite this, the noise and peak broadening problem could not be resolved. Even after background correction by X'pert Highscore plus, the noise and peak broadening are quite prominent from Fig. 3. The noise and peak broadening are attributed to poorly crystalline materials and nanomaterials [64, 66]. The possibility of nanomaterial has been ruled out by analysis. Therefore, the examination of the second possibility arose.

It has been reported that background noise in XRD is due to large amounts of components (e.g., defects) that do not produce XRD peaks, which could rise significantly above the background noise [64, 66]. However, only a smidgeon of noise was detected in the previous investigations [28, 29, 32, 34, 35, 55] of other oxides and their mixtures. The significant noise in XRD may be due to several reasons [64, 66]. The possibility of other reasons (except surface excess oxygen) are ruled out here because the same instrument has carried out all other investigations with the same molybdenum target [28, 29, 32, 34, 35, 55]. As mentioned earlier, the next possibility is the presence of other components or defects (i.e., surface excess oxygen). A stoichiometric oxide doesn't have surface excess oxygen [29, 32, 34, 35, 55]. Therefore, they don't produce background noise. It has been reported that the surface excess oxygen contributes a part of active oxygen in the case of NiO. Surface oxygen doesn't really produce XRD peaks, but it does create surface defects, which give rise to noise in the XRD [64, 66]. The observation of noise in XRD carried out with copper target further supports the presence of surface excess oxygen.

As mentioned earlier, the peak broadening is due to lower crystallinity, indicating non-stoichiometric Ni<sub>1-x</sub>O. The broadened peaks are evident from Fig. 3. These broadened peaks are due to lattice excess oxygen, as observed by Kim et al. [67]. Kim et al. [67] studied the presence of metal vacancy in non-stoichiometric Ni<sub>1-x</sub>O. They found that the peak broadening is due to a deficiency in crystallinity. They ascribed this to the increased nickel vacancy creation/lattice excess oxygen.

It is a well-known fact that if another component is introduced to a unit cell, it changes the unit cell's XRD pattern by shifting the 2θ values. Therefore, if lattice excess oxygen, as depicted by XRD peak broadening, is present in the NiO, it would definitely shift the 2θ values. Therefore, XRD's 2θ values are compared with the 2θ values of the JCPDS file NiO (JCPDS-00-047-1049). The 2θ values of NiO (JCPDS-00-047-1049) and Ni (JCPDS-00-004-0850) are shown in Table 2. The 2θ values and estimated lattice constant of the raw NiO are shown in Table 3. A comparison is made between the 2θ values of NiO used in the current investigation (Table 3) and the JCPDS file for NiO (Table 2). It is found that the first five most intense peaks of the raw NiO (Table 3) are lower than 2θ values of their corresponding peaks of the JCPDS file (Table 2). It can be concluded that the 2θ shift is due to the lattice excess oxygen.

**Table 2.** 2θ values and intensities of JCPDS files of NiO and Ni

NiO (JCPDS-00-047-1049)		Ni (JCPDS-00-004-0850)	
2θ values	Intensities	2θ values	Intensities
19.549	100.0 (220)	20.084	100 (111)
16.911	61.0 (111)	23.224	47 (200)
27.791	35.0 (322)	33.075	21 (220)
32.713	13.0 (311)	39.003	20 (311)
34.211	8.0 (222)	40.811	7 (222)

**Table 3** Lattice parameter of NiO raw material

2 $\theta$	Intensity (%)	Theta/radian	Sin <sup>2</sup> $\theta$	$h^2+k^2+l^2$	C	(hkl)	a/Å	Average a/Å
16.86242	55	0.147125	0.02149	3	0.007163308	111	4.190399	
19.48531	100	0.170009	0.02862	4	0.007156445	200	4.192408	
27.71598	45	0.241822	0.05734	8	0.007168351	220	4.188925	4.187192
32.68532	12	0.285179	0.07914	11	0.007195124	311	4.181124	
34.16566	11	0.298095	0.08626	12	0.007188313	222	4.183104	

If there is a  $2\theta$  shift in XRD, it will definitely cause a change in the lattice constant. Therefore, the lattice constant is compared. The estimated lattice parameter of raw NiO is 4.1872 Å. It is higher than the lattice parameter 4.177 Å, reported in JCPDS-00-047-1049. It can be ascribed to the presence of lattice excess oxygen. This increase of lattice parameter has also been observed by Dubey et al. [68]. They sintered NiO samples from 673 to 1373 K and noticed active oxygen at all temperatures. They reported the increase of lattice constant due to the rise in lattice excess oxygen. However, they didn't estimate the strain. However, in the current investigation, there is a 2.5% increase in the lattice parameter. Kim et al. [67] ascribed this increase to the increased strain effect caused by the increase of nickel vacancies and increased excess lattice oxygen.

From the above XRD analysis of peak broadening, the  $2\theta$  shift to lower angles, increase in lattice parameter, and lattice strain confirm the existence of excess lattice oxygen in raw NiO. XRD also gives evidence of the surface excess oxygen presence due to the ample noise present in XRD. These combined together confirm the presence of active oxygen. On the other hand, Iodometric studies were conducted to further corroborate this.

## Iodometric Studies

In NiO, the active oxygen content was determined by redox iodometric titration using standardized sodium thiosulfate and potassium iodide solution as a titrant and titrand, respectively. The starch solution was used as the endpoint indicator. Keeping in view the accuracy and reproducibility, iodometric studies of NiO were repeated three times. The active oxygen was determined from the difference between total oxygen and stoichiometric oxygen [65, 69, 70]. The active oxygen in NiO was estimated to be 10.47%. The O/Ni ratio is found to be 1.718, implying that sufficient non-stoichiometry exists in the NiO sample due to active oxygen.

The presence of active oxygen in Ni<sub>1-x</sub>O has been reported by various researchers [65, 67, 68, 71–74]. It has been well accepted that NiO is a p-type oxide with a propensity for formation of a high density of nickel vacancies as charge carriers and excess oxygen interstitial atoms, during growth, that renders the crystal non-stoichiometric Ni<sub>1-x</sub>O [75, 76], making O/Ni ratio > 1. Karsthoof et al. [77] pre-annealed NiO in the air at 973, 1373, and 1723 K, and examined after heating in the vacuum in the temperature range between 293 to 773 K. They found excess oxygen (O/Ni ratio > 1) after evacuation upto 773 K. The ratio goes upto 2.5 after evacuation at 298 K. Dubey et al. [68] found O/Ni ratio > 1 for samples prepared below 973 K from Ni(NO<sub>3</sub>)<sub>2</sub>·6H<sub>2</sub>O by thermal decomposition. The excess oxygen of 39.51% was found in the sample prepared at 673 K [68]. Hala et al. [78] prepared a thin film of NiO by DC reactive magnetron

sputtering and reported the O/Ni ratio 1.40–1.41 as a function of discharge oxygen content. Dubey et al. [71] performed the synthesis and thermogravimetric analysis of non-stoichiometric NiO. They concluded that stoichiometry of NiO changes according to sintering temperature; the samples prepared at low temperature have more active oxygen than the samples prepared at a higher temperature. The experimental results and discussions confirm that active oxygen is always present in NiO. The fast reduction is due to NiO's active oxygen, which has been confirmed by wet chemical analysis, thorough XRD analysis, reduction studies, and literature.

With regard to the industrial applicability of plasma processing, a very important metric is the specific enthalpy requirement for a process and weighing this against the conventional equivalent process. The estimated specific enthalpy obtained from Table 1 (power:750 W, H<sub>2</sub> flow rate:150 × 10<sup>-6</sup> m<sup>3</sup> s<sup>-1</sup>, time:300 s) is 32.8 kWh/kg. However, there are several factors to be taken into consideration: (i) the power efficiency of the current reactor is around 60%, and (ii) several pellets can be reduced at once. An example of the reduction of 3 pellets is shown in Fig. 8., which was carried out under the same plasma parameters, which were used for enthalpy estimation earlier. In this case, an average reduction of 89 percent was obtained. After accounting for this factor, the simultaneous reduction of 3 pellets, and the power efficiency of 60%, the specific enthalpy is calculated to be 7.37 kWh/kg Ni, which is quite low when compared to the specific enthalpy of 29.5 kWh/kg obtained for the H<sub>2</sub> reduction of NiO by Lee et al. [24].

However, there will be further reduction in specific enthalpy by selecting appropriate plasma technology, optimizing plasma parameters, and using the designs for large scale [36], etc.

**Fig. 8** Photograph of three pellets during reduction



## Conclusions

The following conclusions may be drawn from the present investigation on the reduction of nickel oxide in hydrogen plasma:

1. Gibbs standard free energy values of NiO → Ni reduction indicate that NiO can be reduced by molecular hydrogen. However, the presence of excited species ( $H_2^*$ , H,  $H^+$ , etc.) makes CHP a more potent reductant.
2. The equilibrium partial pressure of molecular hydrogen required for NiO → Ni reduction decreases with decreasing temperature, thus favoring the low-temperature reduction (below 1500 K). The decrease of equilibrium partial pressure with temperature is much sharper for atomic hydrogen than molecular hydrogen.
3. Active oxygen is present in non-stoichiometric NiO.
4. The presence of active oxygen starts the reduction instantly, which makes the reduction faster.
5. Kinetic rate laws are challenging to apply for NiO reduction due to active oxygen.
6. The NiO → Ni reduction is feasible at least between microwave power 600 W to 750 W,  $H_2$  flow rate  $1.1667 \times 10^{-6} \text{ m}^3 \text{ s}^{-1}$  to  $2.5 \times 10^{-6} \text{ m}^3 \text{ s}^{-1}$ , and sample size  $\sim 2.5 \times 10^{-3}$  to  $\sim 7.5 \times 10^{-3}$  kg.
7. The reduction of  $\sim 7.5 \times 10^{-3}$  kg pellet at such low microwave power and hydrogen flow rate opens up the possibility of CHP's up scalability for NiO reduction.
8. Specific enthalpy is estimated to be 7.37 kWh/kg Ni, which can be lowered further by applying the right plasma technology, optimizing plasma parameters, and applying large scale designs.

**Acknowledgements** I am thankful to Prof. (Dr.) Barada Kanta Mishra, Director, Indian Institute of Technology Goa, India, and Prof. (Dr.) Raja Kishore Paramguru, Professor (Retd.), Mechanical Engineering, KIIT and Chief Scientist (Retd.) CSIR-IMMT, Bhubaneswar, for their guidance throughout my research. I would also like to thank CSIR, New Delhi, for providing financial support to carry out research work under the project MINMET, Project No. ESC 205. Last but not least, I am sincerely thankful to Prof. (Dr.) Seshadri Seetharaman, KTH Royal Institute of Technology, Stockholm (KTH), Sweden, for sharing his immense knowledge and expertise on the reduction of NiO.

## References

1. Meshram P, Abhilash PBD (2019) Advanced review on extraction of nickel from primary and secondary sources. *Miner Process Extr Metall Rev* 40:157–193. <https://doi.org/10.1080/08827508.2018.1514300>
2. Oxley A, Smith ME, Caceres O (2016) Why heap leach nickel laterites? *Miner Eng* 88:53–60. <https://doi.org/10.1016/j.mineng.2015.09.018>
3. Petrus HTBM, Putera ADP, Sugiarto E et al (2019) Kinetics on roasting reduction of limonitic laterite ore using coconut-charcoal and anthracite reductants. *Miner Eng* 132:126–133. <https://doi.org/10.1016/j.mineng.2018.11.043>
4. Zhu D, Pan L, Guo Z et al (2019) Utilization of limonitic nickel laterite to produce ferronickel concentrate by the selective reduction-magnetic separation process. *Adv Powder Technol* 30:451–460. <https://doi.org/10.1016/j.apt.2018.11.024>
5. Garcés-Granda A, Lapidus GT, Restrepo-Baena OJ (2018) The effect of calcination as pre treatment to enhance the nickel extraction from low-grade laterites. *Miner Eng* 120:127–131. <https://doi.org/10.1016/j.mineng.2018.02.019>

6. Rodrigues F, Pickles CA, Peacey J et al (2017) Factors affecting the upgrading of a nickeliforous limonitic laterite ore by reduction roasting, thermal growth and magnetic separation. *Minerals* 7:176. <https://doi.org/10.3390/min7090176>
7. Moats MS, Davenport WG (2014) Nickel and Cobalt Production. In: *Treatise on Process Metallurgy*. 3. Elsevier. 625–669
8. Yang J, Zhang G, Ostrovski O, Jahanshahi S (2019) Selective reduction of an Australian garnieritic laterite ore. *Miner Eng* 131:79–89. <https://doi.org/10.1016/j.mineng.2018.10.018>
9. de Alvarenga OV, dos Santos CG, de Albuquerque BE (2019) Assessing the influence of nacl on the reduction of a siliceous laterite nickel ore under caron process conditions. *Metall Mater Trans B Process Metall Mater Process Sci*. 50:1309–1321 <https://doi.org/10.1007/s11663-019-01552-w>
10. Gomaa MM, Yazdi GR, Schmidt S et al (2017) Effect of precursor solutions on the structural and optical properties of sprayed NiO thin films. *Mater Sci Semicond Process* 64:32–38. <https://doi.org/10.1016/j.mssp.2017.03.009>
11. Fedorov AV, Kukushkin RG, Yeletsky PM et al (2020) Temperature-programmed reduction of model CuO, NiO and mixed CuO–NiO catalysts with hydrogen. *J Alloys Compd* 844:156135. <https://doi.org/10.1016/j.jallcom.2020.156135>
12. Ma B, Xing P, Yang W et al (2017) Solid-state metalized reduction of magnesium-rich low-nickel oxide ores using coal as the reductant based on thermodynamic analysis. *Metall Mater Trans B* 48:2037–2046 <https://doi.org/10.1007/s11663-017-0977-x>
13. Kharchenko Y V, Bliharshkyy ZY, Vira V V, Vasylyv BD (2019) Study of structural changes in a nickel oxide containing anode material during reduction and oxidation at 600°C. In: Fesenko O., Yatsenko L. (eds) *Nanocomposites, Nanostructures, and Their Applications*. Springer Science and Business Media, LLC, Institute of Building and Environmental Engineering, Lviv Polytechnic National University, Lviv, Ukraine [https://doi.org/10.1007/978-3-030-17759-1\\_42](https://doi.org/10.1007/978-3-030-17759-1_42)
14. Bakhshandeha S, Setoudeh N, Ali Askari Zamanic M, Mohassel A (2019) Carbothermic reduction of nickel oxide. *Adv Process Mater Eng* 13(63):75 [https://ma.iaumajlesi.ac.ir/article\\_667347\\_en.html](https://ma.iaumajlesi.ac.ir/article_667347_en.html)
15. Cabascango VEQ, Bazhin VY (2020) Nickel oxide reduction in CO/CO<sub>2</sub> gas mixtures in reverberatory furnaces. In: *J Phys: Conf Ser*. IOP Publishing. 22028 <https://doi.org/10.1088/1742-6596/1515/2/022028>
16. Hidayat T, Rhamdhani MA, Jak E, Hayes PC (2009) The kinetics of reduction of dense synthetic nickel oxide in H<sub>2</sub>–N<sub>2</sub> and H<sub>2</sub>–H<sub>2</sub>O atmospheres. *Metall Mater Trans B Process Metall Mater Process Sci* 40:1–16. <https://doi.org/10.1007/s11663-008-9212-0>
17. Reid JG, Fittock JE (2004) Yabulu 25 years on. In: *International Laterite Nickel Symposium, TMS Annual Meeting, The Minerals, Metals and Materials Society, Charlotte, NC, USA*, pp. 599–618.
18. Utigard TAA, Wu M, Plascencia G, Marin T (2005) Reduction kinetics of goro nickel oxide using hydrogen. *Chem Eng Sci* 60:2061–2068. <https://doi.org/10.1016/j.ces.2004.11.024>
19. Rashed AH, Rao YK (1997) Kinetics of reduction of nickel oxide with hydroge gas in the 230–452°C range. *Chem Eng Commun* 156:1–30. <https://doi.org/10.1080/00986449708936666>
20. Benton AF, Emmett PH (1924) The reduction of nickelous and ferric oxides by hydrogen. *J Am Chem Soc* 46:2728–2737. <https://doi.org/10.1021/ja01677a018>
21. L'vov BV, Galwey AK, L'vov BV, et al. 2012. The mechanism and kinetics of NiO reduction by hydrogen Thermochemical approach. *J Therm Anal Calorim*. 110 601 610. <https://doi.org/10.1007/s10973-011-2000-0>
22. Chatterjee R, Banerjee SSS, Banerjee SSS, Ghosh D (2012) Reduction of nickel oxide powder and pellet by hydrogen. *Trans Indian Inst Met* 65:265–273. <https://doi.org/10.1007/s12666-012-0130-0>
23. Manukyan KV, Avetisyan AG, Shuck CE et al (2015) Nickel oxide reduction by hydrogen: kinetics and structural transformations. *J Phys Chem C* 119:16131–16138. <https://doi.org/10.1021/acs.jpcc.5b04313>
24. Lee DS, Dong, Min J, Min DJ, 2019. A Kinetics of Hydrogen Reduction of Nickel Oxide at Moderate Temperature. *Met Mater Int*. 25 982 990. <https://doi.org/10.1007/s12540-019-00261-y>
25. Yu D, Zhu M, Utigard TA, Barati M (2013) TGA kinetic study on the hydrogen reduction of an iron nickel oxide. *Miner Eng* 54:32–38. <https://doi.org/10.1016/j.mineng.2013.03.018>
26. Zhou Z, Han L, Bollas GM (2014) Kinetics of NiO reduction by H<sub>2</sub> and Ni oxidation at conditions relevant to chemical-looping combustion and reforming. *Int J Hydrogen Energy* 39:8535–8556 <https://doi.org/10.1016/j.ijhydene.2014.03.161>
27. Sabat KC, Rajput P, Paramguru RK et al (2014) Reduction of oxide minerals by hydrogen plasma: an overview. *Plasma Chem Plasma Process* 34:1–23. <https://doi.org/10.1007/s11090-013-9484-2>
28. Rajput P, Sabat KC, Paramguru RK et al (2014) Direct reduction of iron in low temperature hydrogen plasma. *Ironmak Steelmak* 41:721–731. <https://doi.org/10.1179/1743281214Y.0000000186>

29. Sabat KC, Paramguru RK, Pradhan S, Mishra BK (2015) Reduction of Cobalt Oxide ( $\text{Co}_3\text{O}_4$ ) by Low temperature hydrogen plasma. *Plasma Chem Plasma Process* 35:387–399. <https://doi.org/10.1007/s11090-014-9602-9>
30. Sabat KC (2019) Hydrogen Plasma - Thermodynamics. In: *J Phys: Conf Ser. Institute of Physics Publishing*. 1–20 <https://doi.org/10.1088/1742-6596/1172/1/012086>
31. Sabat KC (2019) Iron production by hydrogen plasma. In: *Internat Conf Appl Phys, Pow mater Sci. Institute of Physics Publishing*. 1–5 <https://doi.org/10.1088/1742-6596/1172/1/012043>
32. Sabat KC, Paramguru RK, Mishra BK (2017) Reduction of oxide mixtures of ( $\text{Fe}_2\text{O}_3 + \text{CuO}$ ) and ( $\text{Fe}_2\text{O}_3 + \text{Co}_3\text{O}_4$ ) by low-temperature hydrogen plasma. *Plasma Chem Plasma Process* 37:979–995. <https://doi.org/10.1007/s11090-017-9818-6>
33. Sabat KC (2021) Physics and Chemistry of Solid State Direct Reduction of Iron Ore by Hydrogen Plasma. *Phys Chem Solid State* 22:312–320. <https://doi.org/10.15330/pcss.22.2.292-300>
34. Sabat KC (2019) Formation of CuCo alloy from their oxide mixtures through reduction by low-temperature hydrogen plasma. *Plasma Chem Plasma Process* 39:1071–1086. <https://doi.org/10.1007/s11090-019-09963-y>
35. Sabat KC, Paramguru RK, Mishra BK (2018) Formation of copper–nickel alloy from their oxide mixtures through reduction by low-temperature hydrogen plasma. *Plasma Chem Plasma Process* 38:621–635. <https://doi.org/10.1007/s11090-018-9880-8>
36. Sabat KC, Murphy AB (2017) Hydrogen plasma processing of iron ore. *Metall Mater Trans B Process Metall Mater Process Sci* 48:1561–1594. <https://doi.org/10.1007/s11663-017-0957-1>
37. Liu S-H, Zhang S-L, Li C-X et al (2019) Generation of long laminar plasma jets: experimental and numerical analyses. *Plasma Chem Plasma Process* 39:377–394. <https://doi.org/10.1007/s11090-018-9949-4>
38. Nguyen VT, Murphy AB, Delaney GW, et al (2021) Progress towards a complete model of metal additive manufacturing. In: *Mater Sci Forum. Trans Tech Publications Ltd*. 1031–1038 <https://doi.org/10.4028/www.scientific.net/msf.1016.1031>
39. Mostaghimi J, Boulos MI (2015) Thermal plasma sources: how well are they adopted to process needs? *Plasma Chem Plasma Process* 35:421–436. <https://doi.org/10.1007/s11090-015-9616-y>
40. Mandal AK, Dishwar RK, Sinha OP (2018) Design, fabrication, and characterization of an indigenously fabricated prototype transferred arc plasma furnace. *IEEE Trans Plasma Sci* 46:1793–1799. <https://doi.org/10.1109/TPS.2018.2817234>
41. Souza Filho IR, Ma Y, Kulse M et al (2021) Sustainable steel through hydrogen plasma reduction of iron ore: process, kinetics, microstructure, chemistry. *Acta Mater*. <https://doi.org/10.1016/j.actamat.2021.116971>
42. Saravanakumar R, Ramachandran K, Padmanabhan PVA (2021) Plasma Assisted Aluminothermic Reduction of Cr and Fe Oxides from Chromium Bearing Waste. *Plasma Chem Plasma Process* 41:155–169. <https://doi.org/10.1007/s11090-020-10131-w>
43. Ramos SV, Cisquini P, Nascimento RC Jr et al (2021) Morphological changes and kinetic assessment of  $\text{Cu}_2\text{O}$  powder reduction by non-thermal hydrogen plasma. *J Mater Res Technol* 11:328–341. <https://doi.org/10.1016/j.jmrt.2020.12.038>
44. Mandal AK, Dishwar RK, Sinha OP (2018) Behavior of an indigenously fabricated transferred arc plasma furnace for smelting studies. *Plasma Sci Technol*. <https://doi.org/10.1088/2058-6272/aa9cde>
45. Dishwar RK, Agrawal S, Mandal AK, Sinha OP (2020) Smelting process of chromite ore fines to produce crude Fe–Cr–Ni–N Alloy. *Trans Indian Inst Met* 73:537–542. <https://doi.org/10.1007/s12666-020-01861-8>
46. Mandal AK, Sinha OP (2016) Recovery of multi-metallic components from bottom ash by smelting reduction under plasma environment. *Metall Mater Trans B* 47:19–22. <https://doi.org/10.1007/s11663-015-0484-x>
47. Du C, Qiu R, Ruan J (2018) Scientific and industrial application of plasma fluidized bed. In: *Plasma Fluidized Bed*. Springer. 81–121 [https://doi.org/10.1007/978-981-10-5819-6\\_8](https://doi.org/10.1007/978-981-10-5819-6_8)
48. Samal S (2017) Thermal plasma technology: the prospective future in material processing. *J Clean Prod* 142:3131–3150. <https://doi.org/10.1016/j.jclepro.2016.10.154>
49. Mandal AK, Pramanik S, Sinha OP (2019) Effect of exposure time, lining material and plasma gas on the extraction of aluminium from waste by smelting reduction. *Trans Indian Inst Met* 72:1181–1186. <https://doi.org/10.1007/s12666-019-01602-6>
50. Gleizes A, Cressault Y (2017) Effect of metal vapours on the radiation properties of thermal plasmas. *Plasma Chem Plasma Process* 37:581–600. <https://doi.org/10.1007/s11090-016-9761-y>
51. Ishigaki T (2017) Synthesis of functional oxide nanoparticles through rf thermal plasma processing. *Plasma Chem Plasma Process* 37:783–804. <https://doi.org/10.1007/s11090-017-9788-8>
52. Bazaka K, Baranov O, Cvelbar U et al (2018) Oxygen plasmas: a sharp chisel and handy trowel for nanofabrication. *Nanoscale* 10:17494–17511 <https://doi.org/10.1039/C8NR06502K>



53. Gueroult R, Rax JM, Fisch NJ (2018) Plasma separation for rare earth elements recycling. 45th EPS Conf Plasma Physics, EPS 2018 2018-July:925–928 <http://ocs.ciemat.es/EPS2018ABS/pdf/P2.3013.pdf>
54. Murphy AB (2000) Transport coefficients of hydrogen and argon–hydrogen plasmas. *Plasma Chem Plasma Process* 20:279–297. <https://doi.org/10.1023/A:1007099926249>
55. Sabat KC, Paramguru RK, Mishra BK (2016) Reduction of copper oxide by low-temperature hydrogen plasma. *Plasma Chem Plasma Process* 36:1111–1124. <https://doi.org/10.1007/s11090-016-9710-9>
56. National Institute of Standards and Technology (2012) NIST-JANAF Thermochemical Tables. <https://janaf.nist.gov/>. Accessed 13 Mar 2021
57. Kubaschewski O, Alcock CB (1979) *Metallurgical thermochemistry*, 5th edn. Pergamon Press, Oxford, Newyork <https://doi.org/10.1002/crat.19800150208>
58. Chase M (1998) NIST-JANAF Thermochemical Tables, 4th Edition. *J. Phys. Chem. Ref. Data, Monogr.* 9 1952 <https://doi.org/10.18434/T42S31>
59. Lee H-G (1999) *Chemical thermodynamics for metals and materials*. Imperial college press, London, UK
60. Turkdogan ET (1980) *Physical chemistry of high temperature technology*. Academic Press, Newyork, USA
61. Gamsjäger H, Bugajski J, Preis W, et al (2005) *Chemical thermodynamics of nickel*. Elsevier Amsterdam <https://www.oecdnea.org/dbtdb/pubs/vol6-nickel.pdf>
62. Dieke GH (1958) The molecular spectrum of hydrogen and its isotopes. *J Mol Spectrosc* 2:494–517. [https://doi.org/10.1016/0022-2852\(58\)90095-X](https://doi.org/10.1016/0022-2852(58)90095-X)
63. III RDJ NIST Computational Chemistry Comparison and Benchmark Database, NIST Standard Reference Database Number 101 Release 21, August 2020.. <https://cccbdb.nist.gov/exp2x.asp?casno=1333740&charge=0>
64. Cullity SR, Stock BD (2001) *Elements of x-ray diffraction*. Prentice Hall, USA
65. Dereñ J, Stoch J (1970) Effect of biography on stoichiometric composition and chemisorptive properties of nickel oxide (oxygen chemisorption). *J Catal* 18:249–259. [https://doi.org/10.1016/0021-9517\(70\)90319-2](https://doi.org/10.1016/0021-9517(70)90319-2)
66. Holder CF, Schaak RE (2019) Tutorial on Powder X-ray Diffraction for Characterizing Nanoscale Materials. *ACS Nano* 13:7359–7365. <https://doi.org/10.1021/acsnano.9b05157>
67. Soo Kim D, Chul Lee H (2012) Nickel vacancy behavior in the electrical conductance of nonstoichiometric nickel oxide film. *J Appl Phys.* 112: 034504 <https://doi.org/10.1063/1.4742993>
68. Dubey P, Kaurav N, Devan RS et al (2018) The effect of stoichiometry on the structural, thermal and electronic properties of thermally decomposed nickel oxide. *RSC Adv* 8:5882–5890 <https://doi.org/10.1039/c8ra00157j>
69. Dereñ J, Mrowec S (1973) Semiconducting and transport properties of mono- and polycrystalline nickel oxide. *J Mater Sci* 8:545–558. <https://doi.org/10.1007/BF00550459>
70. Dereñ J, Nowotny J (1969) Mechanism and kinetics of interaction between gaseous oxygen and nickel oxide surfaces. *Oxid Met* 1:73–91. <https://doi.org/10.1007/BF00609925>
71. Dubey P, Kaurav N (2017) Synthesis and thermogravimetric analysis of non-stoichiometric nickel oxide compounds. *J Phys Conf Ser.* 839: 012040 <https://doi.org/10.1088/1742-6596/836/1/012040>
72. Bielański A (1979) Oxygen in catalysis on transition metal oxides. *Catal Rev* 19:1–41. <https://doi.org/10.1080/03602457908065099>
73. Yang R, Zhang D, Zhu K et al (2019) In situ study of the conversion reaction of Co<sub>2</sub> and Co<sub>2</sub>-H<sub>2</sub> mixtures in radio frequency discharge plasma. *Wuli Huaxue Xuebao/ Acta Phys - Chim Sin* 35:292–298. <https://doi.org/10.3866/PKU.WHXB201803121>
74. Dubey P, Kaurav N (2019) *Stoichiometric and Nonstoichiometric Compounds*. IntechOpen. <https://doi.org/10.5772/intechopen.89402>
75. Passerini S, Scrosati B (1994) Characterization of nonstoichiometric nickel oxide thin-film electrodes. *J Electrochem Soc* 141:889–895. <https://doi.org/10.1149/1.2054853>
76. Pizzini S, Morlotti R (1967) Thermodynamic and transport properties of stoichiometric and nonstoichiometric nickel oxide. *J Electrochem Soc* 114:1179–1189. <https://doi.org/10.1149/1.2426441>
77. Karsthof R, Anton AM, Kremer F, Grundmann M (2020) Nickel vacancy acceptor in nickel oxide: doping beyond thermodynamic equilibrium. *Phys Rev Mater* 4:1–9. <https://doi.org/10.1103/PhysRevMaterials.4.034601>
78. Hala M, Capek J, Zabeida O et al (2012) Hysteresis-free deposition of niobium oxide films by HiPIMS using different pulse management strategies. *J Phys D Appl Phys* 45:1–28. <https://doi.org/10.1088/0022-3727/45/5/055204>